

An Improved BRDF Hotspot Model and its Use in VLIDORT to Study the Impact of Atmospheric Scattering on Hotspot Directional Signatures in the Atmosphere

Xiaozhen Xiong^{1*}, Xu Liu¹, Robert Spurr²,
Ming Zhao^{1,3}, Qiguang Yang^{1,3}, Wan Wu¹, Liqiao Lei^{1,3}

¹NASA Langley Research Center, Hampton, VA, USA

²RT SOLUTIONS Inc., Cambridge, MA, USA

³Adnet Systems Inc., Bethesda, MD 20817, USA

Corresponding to: Xiaozhen Xiong (Xiaozhen.Xiong@nasa.gov)

Abstract

The term “hotspot” refers to the sharp increase of reflectance occurring when incident (solar) and reflected (viewing) directions **almost** coincide in the backscatter direction. The accurate simulation of hotspot directional signatures is important for many remote sensing applications. The RossThick-LiSparse-Reciprocal (RTLSR) Bidirectional Reflectance Distribution Function (BRDF) model is widely used in radiative transfer simulations, **and the hotspot model mostly used is from Maignan- Bréon** but it typically requires large values of numerical quadrature and Fourier expansion terms in order to represent the hotspot accurately **for its use coupled with atmospheric radiative transfer modelling (RTM)**. In this paper, we have developed a **modified version based on the Maignan- Bréon’s hotspot BRDF model that converges much faster numerically, making it more practical for use in the RTMs that require Fourier expansion of BRDF to simulate the top-of-atmosphere (TOA) hotspot signatures, such as in the RTM models using Doubling-Adding or discrete ordinate method. Using the vector linearized discrete ordinate radiative transfer model (VLIDORT), we found that reasonable TOA hotspot accuracy can be obtained with just 23 Fourier terms for clear atmospheres, and 63 Fourier terms for atmospheres with aerosol scattering.**

In order to study to the impact of molecular and aerosol scattering on hotspot signatures, we carried out a number of hotspot signature simulations with VLIDORT. We confirmed that (1) atmospheric molecules scattering and the existence of aerosol tend to smooth out the hotspot signature at the TOA, but has no impact on hotspot width; and (2) the hotspot signature at the TOA in the near-infrared is larger than in the visible, and its impact by surface reflectance is more significant. As the hotspot amplitude at the TOA with aerosol scattering included is smaller than that with molecular scattering only, the amplitude of hotspot signature at the surface is likely underestimated in the previous analysis based on the POLDER measurements, where the atmospheric correction was based on a single-scatter Rayleigh-only calculation. We also draw attention to a scaling factor of $3\pi/4$ which has been applied to the Ross-Thick kernel with hotspot correction. This modified model can calculate the amplitude of hot spot accurately, and, as it agrees very well with the original RossThick model away the hotspot region, this model can be simply used in conditions with and without hotspot. However, there are some differences of this modified model with the

Formatted: Subscript

Formatted: Justified, Space After: 0 pt, Don't adjust space between Latin and Asian text, Don't adjust space between Asian text and numbers

Deleted: I

Deleted: ,

Deleted: n improved

Deleted:

Deleted: s

Deleted: atmospheric radiative transfer

Deleted: ions of

Deleted: . Using

Deleted: RT model

Deleted: ¶

Deleted: W

Deleted: to study to the impact of molecular and aerosol scattering on hotspot signatures

Deleted: s

Formatted: Strikethrough

Deleted: has an obvious increase with the solar zenith angle

Deleted: attenuation

Formatted: Strikethrough

Formatted: Strikethrough

Formatted: Strikethrough

62 original Maignan- Bréon model for the scattering angles close to the hot spot point, thus it may
63 not be appropriate for those who need an exact representation of the Hot Spot angular signature.

Formatted: Font: (Default) Times New Roman, 12 pt

64
65
66
67
68
69 Keywords: BRDF, Hot Spot, VLIDORT, RTLSR
70
71
72
73
74

75 1. Introduction

76 Most land surfaces reflect incident light anisotropically. For a given incident sun angle, the surface
77 reflectance may vary by a factor of two in the near infrared [Kriebel et al., 1978]. An accurate
78 accounting of the anisotropic reflectance at the Earth's surface is very important for many remote
79 sensing applications, including monitoring of climate changes, mapping land covers, analyzing
80 vegetation densities, or inter-calibration between different satellite instruments (e.g. [Yang et al.,
81 2020] and references therein). Lorente et al. [2018] investigated the importance of surface
82 reflectance anisotropy with regard to cloud and NO₂ retrievals from satellite measurements by the
83 Global Ozone Monitoring Experiment 2 (GOME-2) and the Ozone Monitoring Instrument (OMI).
84 This study showed that retrieved cloud fractions have an east–west across-track bias of 10-50 %,
85 and under moderately polluted NO₂ scenarios with backward scattering geometry, clear-sky air
86 mass factors can be as much as 20% higher when surface anisotropic reflection is included in the
87 calculations.

88 The angular distribution of reflected light by a surface is normally represented mathematically by
89 the Bidirectional Reflectance Distribution Function (BRDF) [Nicodemus et al., 1992], which is a
90 function of the incident solar zenith angle, the reflected viewing zenith angle, and the relative
91 azimuth angle between these two directions. Usually, there is a strong increase in BRDF toward
92 the back^ward-scatter direction, with much smaller BRDF variations seen around the opposite
93 forward-scatter direction. Peak BRDF values occur when backscatter incident and reflected
94 directions coincide; this sharp reflectance increase is usually referred to as the “hotspot” [Kuusk,
95 1985; Hapke, 1986]. The “hotspot” effect has been observed for a variety of planetary bodies,
96 including the Moon, Mars, asteroids, planetary satellites, as well as terrestrial vegetation [Bréon
97 et al., 2002]. The most widely accepted explanation for the hotspot effect is the so-called “shadow
98 hiding” effect. Here, particles at the surface (e.g. leaves, soil grains) cast shadows on adjacent
99 particles; these shadows are visible at large phase angles but at zero phase angle the shadows are
100 hidden by the particles that cast them. Coherent backscatter is another physical explanation of
101 reflectance enhancement in the hotspot direction [Kuga and Ishimaru, 1984; Hapke et al., 1993].

Formatted: Font color: Text 1

102 The bidirectional reflective spectra of land surfaces have been measured in laboratories, fields and
103 airborne experiments, or derived from satellite observations. The two most widely used
104 hyperspectral bidirectional reflective spectra of land surfaces are (1) the U.S. Geological Survey
105 (USGS) Spectral Library (Version 7) [Kokaly et al., 2017], comprising a very diverse land surface
106 BRDF data based with about 40,000 spectra in all, and (2) the ASTER Spectral Library from

107 NASA's Jet Propulsion Laboratory, with a collection of over 2,000 measured spectra [Baldridge
108 et al., 2009]. Using these two databases and Ross-Thick-Li-Sparse-Reciprocal (RTLSR model),
109 Yang et al. [2020] went on to develop a Hyper-Spectral Bidirectional Reflectance (HSBR) model
110 for remote sensing applications. BRDF data derived from satellite observations have been used to
111 evaluate and correct for anisotropy in several instruments, including, for example, the Advanced
112 Very High Resolution Radiometer (AVHRR) [e.g. Gutman, 1987; Roujean et al., 1992], the
113 Along-Track Scanning Radiometer (ATSR-2) located on board on the ERS-2 platform [Godsalve,
114 1995], and the MODerate resolution Imaging Spectrometer (MODIS) [Wanner et al., 1997; Lucht
115 et al., 2000; Schaaf et al., 2002]. However, the AVHRR, ATSR and MODIS instruments have
116 limited viewing geometry options; in contrast, the POLarization and Directionality of Earth
117 Reflectances (POLDER) instrument on board the Advanced Earth Observing Satellite (ADEOS)
118 in August 1996 provided a much better directional sampling to measure the BRDF up to 65° VZA
119 (viewing zenith angle) and for the full azimuth range [Deschamps et al., 1994]. So, these POLDER
120 reflectance measurements were used to examine the hotspot signature for different vegetated
121 surfaces [Bréon et al., 2002].

122 Many BRDF models have been developed in order to simulate or reproduce directional signatures
123 of land surface reflectance. These include empirical models [Walthall et al., 1985], semi-empirical
124 models [Hapke, 1981, 1986; Rahman et al., 1993; Roujean et al., 1992; Wanner et al., 1995; 1997;
125 Lucht et al., 2000], and physical models [Pinty and Verstraete, 1991]. In particular, kernel-driven
126 semi-empirical models have been used frequently to generate global BRDF and albedo products.
127 Several studies have identified the so-called Ross-Thick-Li-Sparse-Reciprocal (hereinafter
128 "RTLSR") kernel combination as the BRDF model best suited for the operational MODIS
129 BRDF/Albedo algorithm [Wanner et al., 1997; Lucht et al., 2000; Schaaf et al., 2002]. Using about
130 22,000 sets of the measured BRDFs derived from carefully selected cloud-free measurements with
131 large directional coverage from the spaceborne POLDER instrument [Bicheron and Leroy, 2000],
132 Maignan et al. [2004] evaluated the efficacy of several analytical models to reproduce these
133 observed BRDF signatures. They found that a simple kernel-driven model with only three free
134 parameters can provide an accurate representation of the BRDF. One of the best such models is
135 the three-parameter linear Ross-Li model. However, this model fails to capture the sharp
136 reflectance increase centered around the hotspot backscatter direction. From an analysis of
137 POLDER data, a correction to this model to capture the hotspot effect was proposed by [Bréon et
138 al., 2002]. By means of an explicit representation of the hotspot effect for a few degrees around
139 the backscattering direction, Maignan et al. [2004] found that the hot-spot modified RTLSR linear
140 BRDF model with three free parameters produced the best agreement with measurement. This
141 BRDF model from [Maignan et al., 2004] was referred to as the "Ross-Li-Maignan" model in
142 [Vermeote et al., 2009].

143 With three linear parameters characterizing the Ross-Li model, it is a straightforward process to
144 invert the model by minimizing the Root Mean Square (hereafter RMS) difference between the
145 measurements and the modeled directional reflectances. This BRDF inversion technique has been
146 used to derive the MODIS BRDF/Albedo product [Schaaf et al., 2002]. An improvement was made
147 by Vermeote et al. (2009) to correct the time series of surface reflectance derived from MODIS.
148 Using POLDER data, Bacour and Bréon [2005] retrieved the three parameters, using the modified
149 Ross-Li model, and further analyzed the variability of these parameters with vegetation cover
150 types. A common approach to derive the surface reflectance directional signatures from satellite
151 observations is to first remove the atmospheric absorption and scattering effects. This process,
152 which converts the top of the atmosphere (TOA) signal to a surface reflectance, is often called

Formatted: Font: Times New Roman, 12 pt

Deleted: n

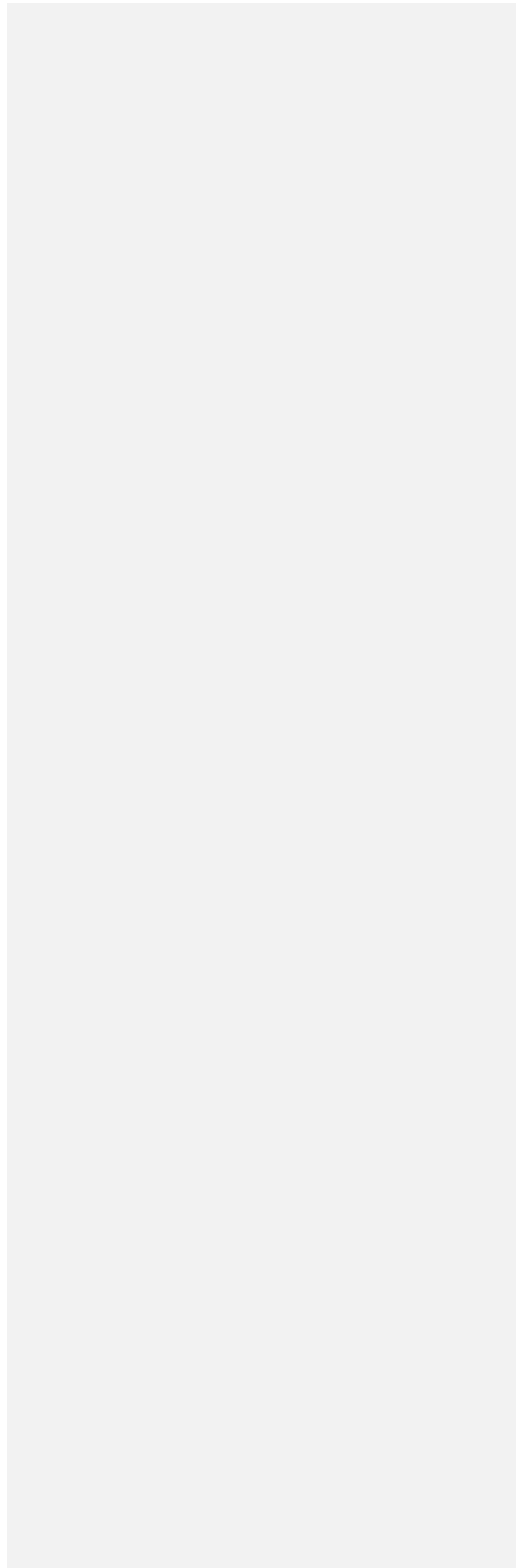
Deleted: n

155 “atmospheric correction”. The surface is generally taken to be Lambertian in such atmospheric
156 correction algorithms; however, it was found that without considering the BRDF effects,
157 atmosphere correction errors can reach up to 10% at certain geometries and under turbid conditions
158 [Vermote et al., 1997]. Since the mid-1980s, atmospheric correction algorithms have evolved from
159 the earlier “empirical line” and “flat-field” methods to more modern approaches based on rigorous
160 radiative transfer modeling [Gao et al., 2009]. Clearly, the accurate simulation of atmospheric and
161 surface radiative transfer is a critical element in the derivation of surface BRDF from satellite
162 measurements.

163 Several key numerical radiative transfer models (RTMs) were developed in the 1980s, and the
164 most popular RTMs in use today are usually based on discrete ordinate methods or the doubling-
165 adding technique. Following detailed mathematical studies made by Hovenier and others
166 [Hovenier and van der Mee, 1983; de Rooij and van der Stap, 1984], a general doubling-adding
167 model was developed for atmospheric radiative transfer modeling, e.g. [de Haan et al., 1987;
168 Stammes et al., 1989]. DISORT is a discrete ordinate model developed by Stammes and co-
169 workers and released for public use in 1988 [Stammes et al., 1988; Stammes et al., 2000]; a vector
170 discrete ordinate model (VDISORT) was developed later on in the 1990s [Schulz et al., 1999]. In
171 the 1980s, Siewert and colleagues made a number of detailed mathematical examinations of the
172 vector RT equations. The development of the scattering matrix in terms of generalized spherical
173 functions was reformulated in a convenient analytic manner [Siewert, 1981; Siewert, 1982;
174 Vestrucci and Siewert, 1984], and a new and elegant solution from a discrete ordinate viewpoint
175 was developed for the scalar [Siewert, 2000a] and vector [Siewert, 2000b] single-layer slab
176 models. LIDORT [Spurr et al., 2001; Spurr, 2002] and VLIDORT [Spurr, 2006] are multiple-
177 scattering multi-layer discrete ordinate scattering codes with simultaneous linearization facilities
178 for the generation of the radiation field and analytically-derived Jacobians (weighting functions or
179 partial derivatives of the radiation field with respect to any atmospheric or surface parameter).
180 SCIATRAN is a comprehensive software package for the modeling of radiative transfer processes
181 in the terrestrial atmosphere and ocean from the ultraviolet to the thermal infrared, including
182 multiple scattering processes, polarization, thermal emission and ocean-atmosphere coupling; the
183 software package contains several radiative transfer solvers including discrete-ordinate techniques
184 [Rozanov et al., 2014]. The Second Simulation of the Satellite Signal in the Solar Spectrum (6S)
185 [Vermote et al., 1997] RTM is widely used in the atmospheric correction community; 6S is based
186 on the successive orders of scattering approach (SOS) [Lenoble et al., 2007]. In this study, we will
187 use the VLIDORT RTM, which has a fully-developed supplemental code package for the
188 generation of surface BRDFs. This supplement includes a variety of BRDF kernel models (semi-
189 empirical BRDF functions developed for particular types of surfaces) that can be combined
190 linearly to that provide total BRDFs required as input for the full VLIDORT RTM calculations.
191 These kernels include the Ross-Li model both with and without the hotspot correction.

192 In the first part of this study (Section 2) we discuss the Ross-Li kernel hotspot correction in detail,
193 and present an alternative model of the hotspot correction; this new formulation is designed to
194 improve the hotspot convergence with respect to the number of cosine-azimuth Fourier terms
195 needed to represent the BRDF and also to the number of azimuth quadrature angles needed for the
196 numerical derivation of these Fourier terms. In Section 3, we investigate accuracies for
197 reconstructed BRDFs in the hotspot region, comparing our new model with older hot-spot
198 corrections. Then, using VLIDORT and the new hotspot correction model, we examine the impact
199 of atmospheric scattering on the simulated TOA-hotspot signature. Summary and conclusions are
200 given in Section 4.

Deleted: 5



2. Hotspot BRDF Models

2.1. RossThick-LiSparse-Reciprocal (RTLSR) BRDF model

Land surfaces possess complicated structural elements, making the reflective properties of such surfaces very hard to model. The geometric structure of a given land surface greatly influences its reflectance, thanks to shadowing and multiple scattering effects [Roujean et al., 1992]; this angle-dependent scattering component is called “geometric scattering”. Another structure-related scattering effect is called “volumetric scattering”, which usually consists of multiple reflections from different components within a volume and produces a minimum reflectance near nadir viewing. Scattering by trees, branches, soil layers, and snow layers are typical manifestations of volumetric scattering. These two scattering processes are usually used to characterize the surface BRDF. For example, the operational Moderate Resolution Imaging Spectroradiometer (MODIS) BRDF/Albedo product is derived based on semi-empirical kernel-driven linear BRDF models that composes of three components: an isotropic scattering term, a geometric scattering kernel, and a volumetric scattering kernel. The RossThick-LiSparse-Reciprocal (RTLSR) kernel combination has been identified as the best model suited for the operational MODIS BRDF/Albedo retrieval ([Schaaf et al., 2002] and references therein), in which the land surface reflectance function $B(\theta_i, \theta_r, \Delta\varphi)$ is represented as:

$$B(\theta_i, \theta_r, \Delta\varphi) = P_1 K_{Lamb} + P_2 K_{geo}(\theta_i, \theta_r, \Delta\varphi, P_4, P_5) + P_3 K_{vol}(\theta_i, \theta_r, \Delta\varphi). \quad (1)$$

Here, θ_i and θ_r are the incident (solar) and reflected (viewing) zenith angles, and φ_i and φ_r the corresponding azimuth angles, with $\Delta\varphi = \varphi_r - \varphi_i$ the relative azimuth angle. P_1 is the Lambertian kernel amplitude with $K_{Lamb} \equiv 1$, while P_2 and P_3 are the weights of the Li-Sparse-Reciprocal geometric scattering kernel K_{geo} and the Ross-Thick volume scattering kernel K_{vol} respectively. Parameters P_4 and P_5 characterize K_{geo} and are discussed below. This 3-kernel semi-empirical model has shown surprising ability to reproduce with high accuracy the measured directional signatures of the main land surfaces; the RTLSR model is significantly better than other analytical models or combinations thereof [Maignan et al., 2004]

The Li-Sparse-Reciprocal geometric scattering kernel was derived from surface scattering and the theory of geometric shadow casting by [Li and Strahler, 1992], and is given by

$$K_{geo}(\theta_i, \theta_r, \Delta\varphi, P_4, P_5) = \frac{1 + \sec\theta_r' \sec\theta_i' + \tan\theta_r' \tan\theta_i' \cos\Delta\varphi}{2} + \left(\frac{t - \sin t \cos t}{\pi} - 1\right) (\sec\theta_r' + \sec\theta_i'). \quad (2)$$

$$\cos^2 t = \left(\frac{P_4}{\sec\theta_r' + \sec\theta_i'}\right)^2 [G(\theta_r', \theta_i', \Delta\varphi)^2 + (\tan\theta_r' \tan\theta_i' \sin\Delta\varphi)^2]; \quad (3)$$

$$G(\theta_r', \theta_i', \Delta\varphi) = \sqrt{\tan^2\theta_r' + \tan^2\theta_i' - 2\tan\theta_r' \tan\theta_i' \cos\Delta\varphi}; \quad (4)$$

$$\tan\theta_r' = P_5 \tan\theta_r; \quad \tan\theta_i' = P_5 \tan\theta_i. \quad (5)$$

We note also the following expression for the scattering angle ζ :

$$\cos\zeta = \cos\theta_r \cos\theta_i + \sin\theta_r \sin\theta_i \cos\Delta\varphi \quad (6)$$

Assuming a dense leaf canopy, and tree crowns that are spheroids with vertical length $2b$,

Formatted: Font: Times New Roman, 12 pt

Formatted: Font: Times New Roman, 12 pt

Formatted: Font: Times New Roman, 12 pt

horizontal width $2r$, and centroid distance h above the ground, then $P_4 = h/b$ and $P_5 = b/r$ are two parameters representing the crown relative height. P_4 and P_5 can be obtained empirically, and they are usually assumed to take values 2 and 1 respectively.

The Ross-Thick volume scattering kernel K_{vol} was derived from volume scattering radiative transfer models by [Ross, 1981], and it is often referred to as “Ross thick” [Wanner et al., 1995]:

$$K_{vol}(\theta_i, \theta_r, \Delta\varphi) = \frac{\left(\frac{\pi}{2} - \zeta\right) \cos\zeta + \sin\zeta}{\cos\theta_r' + \cos\theta_i'} - \frac{\pi}{4}. \quad (7)$$

Since we are using the RTLSR linear model to reproduce natural target BRDFs, it follows that the three parameters will contain most of the reflectance directional information for view angles of less than 60° . Theoretically, parameter P_1 and P_2 in Eq. (1) can be derived, but due to the extensive variability of surface cover and biome types, there remains the practical question as to the determination of the free parameters [Verote et al., 2009], and for the MODIS BRDF/Albedo product, P_1 , P_2 and P_3 are derived from MODIS measurements in a few channels. A hyperspectral bidirectional reflectance (HSBR) model for land surface was developed by [Yang et al., 2020]. The HSBR model includes a diverse land surface BRDF database with about 40,000 spectra, stored in terms of the three Ross-Li parameters. The HSBR model has been validated using the USGS vegetation database and the AVIRIS reflectance product, and can be used to generate hyperspectral reflectance spectra at different sensor and solar observation geometries.

2.2. Hot-Spot models, including an improved formulation

Based on an analysis of POLDER measurements, Bréon et al.[2002] found that the hotspot directional signature is proportional to $(1 + \zeta/\zeta_0)^{-1}$, where ζ_0 is the hotspot halfwidth that can be related to the ratio of scattering element size and canopy vertical density. This hotspot modeling has been validated against measurements acquired with the spaceborne POLDER instrument with a very high directional resolution, i.e. on the order of 0.3° [Bréon et al., 2002]. Maignan et al.[2004] brought this hotspot correction into the Ross-Li model, and re-wrote the Ross thick kernel with hotspot correction as:

$$K_{vol} = \frac{4}{3\pi} \frac{\left(\frac{\pi}{2} - \zeta\right) \cos\zeta + \sin\zeta}{\cos\theta_r' + \cos\theta_i'} \left(1 + \frac{1}{1 + \zeta/\zeta_0}\right) - \frac{1}{3}. \quad (8)$$

We note here that there is a difference of a factor of $\frac{4}{3\pi}$ between Eqs. (7) and (8). Bréon et al. [2002] indicated that ζ_0 is generally in a small range between 0.8° to 2° , while some dispersion occurs in the range 1° – 4° for scenarios classified as forest and desert types in the International Geosphere-Biosphere Program (IGBP) system. For the sake of simplicity, and to avoid the addition of a free parameter in the BRDF modeling, Maignan et al.[2004] suggested setting a constant value of $\zeta_0 = 1.5^\circ$. The version of the RTLSR model which accounts for the hotspot signature using Eq. (8) will be denoted as RossThickHT-M in this paper. Using multidirectional PARASOL (Polarization & Anisotropy of Reflectances for Atmospheric Sciences coupled with Observations from a Lidar) data at coarse resolution (6 km) over a large set of representative targets, Maignan et al.[2004] showed that the simple three-parameter model permits accurate representation of the BRDFs.

Another hotspot correction was developed by Chen and Cihlar[1997] as a negative exponential

Deleted: n

278 function, and Jiao et al. [2013] brought this latter correction to the Ross-Li model, as follows:

279
$$K_{vol} = \frac{4}{3\pi} \frac{\left(\frac{\pi}{2} - \zeta\right) \cos \zeta + \sin \zeta}{\cos \theta'_r + \cos \theta'_i} \left(1 + C_1 e^{\left(-\frac{\zeta}{\pi}\right) C_2}\right) - \frac{1}{3}. \quad (9)$$

280 Here, C_1 is physically related to the difference between the spectral reflectance of foliage and the
281 background, controlling the height of the hotspot; C_2 is related to the ratio of canopy height to the
282 size of the predominant canopy structure, determining the width of the hotspot. We found that we
283 can simply set C_2 to be ζ_0 . We remark that ζ_0 is given in radians in Eq. (8) and in degrees in Eq.
284 (9). However, Bréon et al. [2002] determined that observed hotspot signatures are better fitted with
285 a function of $(1 + \zeta/\zeta_0)^{-1}$ rather than with a negative exponential that is often used for hotspot
286 modeling.

287 In this paper, we denote the version of the RTLSR model that accounts for the Hot-Spot process
288 using Eq. (9) as RossThickHT-C. Some validation to the RossThickHT-C model has been made
289 by Jiao et al. [2013]. Although one advantage of RossThickHT-C model is the ability to use
290 parameter C_1 to adjust the amplitude of hotspot [Jiao et al., 2013], such an adjustment can be also
291 easily made by adding one parameter in the correction term in Eq. (8), i.e. to change $(1 + \zeta/\zeta_0)^{-1}$
292 to $C_1/(1 + \zeta/\zeta_0)$. With this in mind, our effort will focus on an improvement in the Ross-Thick
293 BRDF kernel, starting with the baseline model of Maignan et al. [2004].

294 A number of kernel BRDF models have been incorporated in the LIDORT and VLIDORT RTMs,
295 including the RTLSR model and the RossThickHT-M model. In VLIDORT (and this applies
296 equally to other polarized radiative transfer models). It is necessary to develop solutions for the
297 radiation fields in terms of Fourier cosine and sine azimuth series; the same considerations apply
298 to the BRDFs. For scalar kernel models without polarization, only the Fourier cosine series is
299 needed. The Fourier components of the total BRDF are calculated through:

300
$$B^m(\mu, \mu') = \frac{1}{2\pi} \int_0^{2\pi} B(\mu, \mu', \varphi) \cos m\varphi d\varphi. \quad (10)$$

301 Integration over the azimuth angle is done by double numerical quadrature over the ranges $[0, \pi]$
302 and $[-\pi, 0]$. The number of BRDF azimuth quadrature abscissa (N_{BRDF}) should be set to at least
303 100 in order to obtain a numerical accuracy of 10^{-4} for most kernels considered in the VLIDORT
304 BRDF supplement [Spurr, 2004]. However, at and near the hotspot region, many more quadrature
305 points and Fourier terms ($N_{FOURIER}$) will be needed, as we will demonstrate below. Indeed, Lorente
306 et al. (2018) found that in order to reach an accuracy of 10^{-3} over the hotspot region, 720 Gaussian
307 points were needed for the azimuth integration and 300 Fourier terms for the reconstruction of any
308 BRDF in terms of its Fourier components; they also determined that, in the final implementation
309 of the surface BRDF in the DAK radiative transfer model (Doubling-Adding KNMI, [Lorente et
310 al., 2017]) designed to perform with optimal simulation time, some 100 Fourier terms and 360
311 Gaussian points were necessary for proper hotspot characterization.

312 These values of N_{BRDF} and $N_{FOURIER}$ are still unacceptably high, and in order to use VLIDORT to
313 simulate the hotspot signature with a modest number of discrete ordinates, we have made an
314 empirical modification to the hotspot correction in the RossThickHT-M model by choosing the
315 function with a smooth transition near the hotspot peak and considering $\sin(\zeta)$ can be used to
316 replace ζ approximately when the phase angle is a small value. We experimented with different
317 powers of this function, finally coming up with a function of $\sin^x(\zeta) * \frac{1}{\sin^x(\zeta_0)}$ to replace ζ/ζ_0 ,

Deleted: z

Deleted: i

Formatted: Font: Not Bold, Not Italic

Deleted: by using the

321 where $x = 2 + \sin(\theta_r')$. Thus:

322
$$K_{vol} = \frac{4}{3\pi} \frac{(\frac{\pi}{2} - \zeta) \cos \zeta + \sin \zeta}{\cos \theta_r' + \cos \theta_i'} \left(1 + \frac{1}{1 + \sin^x(\zeta) * \frac{1}{\sin^x(\zeta_0)}} \right) - \frac{1}{3}. \quad (11)$$

323 We use the nomenclature RossThickHT-X to indicate the model with the hotspot correction given
324 in Eq. (11).

325 In the next section, we first examine the above sets of hotspot signatures, with particular emphasis
326 on the accuracy of reconstructed BRDFs in terms of the two numerical indices N_{BRDF} and $N_{FOURIER}$.
327 We then determine the impact of a scattering atmosphere, using these hotspot BRDF quantities as
328 inputs to VLIDORT calculations based on standard-atmosphere pressure/temperature profiles with
329 two cases, one is Rayleigh scattering only and another one with aerosols added. Aerosol is in the
330 form of an optically-constant layer from the surface to 3.0 km with the total optical depth of 0.2,
331 and aerosol optical properties are taken from a “continental pollution” aerosol type [Hess et al.,
332 1998], with lognormal poly-disperse size distribution. Please note that the use of an optical depth
333 of 0.2 for aerosol might be a little high than the background aerosol.

Deleted: 6.5

Deleted: having

Deleted: ;

Formatted: Font: Not Italic

337 **3. Results and Discussion**

338 *3.1 Hotspot Comparisons and BRDF reconstruction accuracy*

339 Figure 1 shows a comparison of the volume-scattering kernel for the three hotspot models,
340 RossThickHT-X, RossThickHT-C and RossThickHT-M, with actual hotspots at three different
341 solar zenith angles in the principal-plane backscatter direction. For reference, the original
342 RossThick kernel is also plotted. The heights of Hotspot peaks from the three models are the same,
343 and the hotspot peak is higher and narrower at larger zenith angles. For model RossThickHT-X,
344 the angular shape around the hot spot peak (VZA=SZA) is not so sharp as the reference model
345 RossThickHT-M, thus, it may not be appropriate for those who need an exact representation of the
346 hot spot angular signature. However, from limited validation Jiao et al. [2013] found that
347 RossThickHT-M apparently overestimates the hot spot magnitude, and RossThickHT-M looks too
348 sharp from Figure 2 of Jiao et al. [2013]. Another major difference between the three models are
349 outside the hotspot region. As indicated by [Jiao et al., 2013], one asset of RossThickHT-C is that
350 it better matches the RossThick model in regions beyond the hotspot, while on the other hand,
351 there remain some differences between the RossThickHT-M and RossThick model away from the
352 hotspot. Our new model RossThickHT-X has the same advantage as RossThickHT-C, in that
353 agreement with the standard RossThick model beyond the hotspot region is accurate, thus
354 RossThickHT-X can be used automatically in conditions with and without hot spot impact and do
355 not to switch the BRDF models from RossThick to the one with HT correction, i.e. RossThickHT-
356 M, when the hot spot occurs.

Formatted: Font: (Default) Times New Roman, 12 pt

Formatted: Font: (Default) Times New Roman, 12 pt

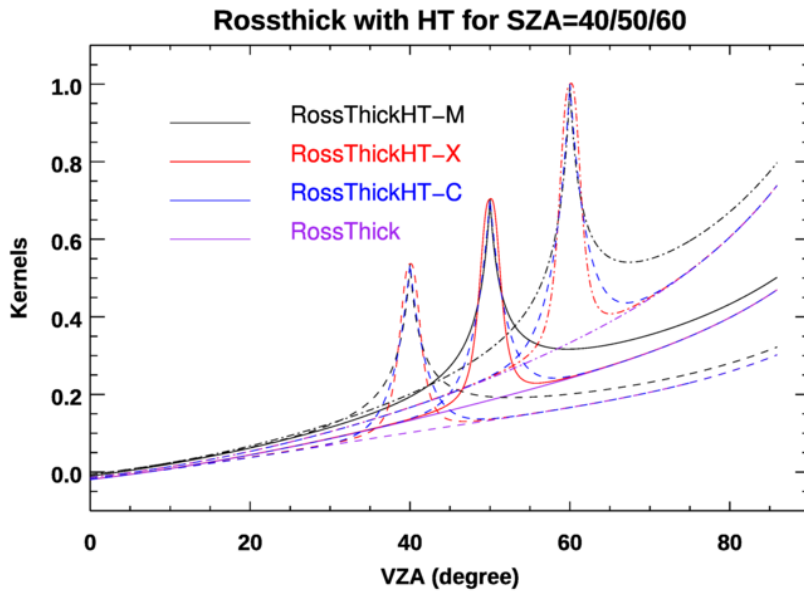
Formatted: Font: (Default) Times New Roman, 12 pt

Deleted: M

Deleted: s

Deleted: .

357



358

362

363 **Figure 1.** Four Ross-Thick volume scattering kernels for a range of reflection zenith angles,
364 and for three solar incident angles as indicated; reflectance is in the principal plane.

365 The major advantage of our new hotspot correction model is the rapid convergence for
366 reconstruction. Table 1 lists values of N_{BRDF} (number of azimuth quadrature abscissae) and
367 $N_{FOURIER}$ (number of Fourier Terms) that are needed to reconstruct the BRDF to different accuracy
368 levels; the accuracy is computed as the relative difference of the reconstructed BRDF to its exact
369 value at the hotspot. Compared to numbers required for the RossThickHT-M, values of N_{BRDF} and
370 $N_{FOURIER}$ for the RossThickHT-X case are 10 to 60 times smaller (Table 1). These results show
371 that RossThickHT-X converges much faster than RossThickHT-M. We see also that convergence
372 of RosstthickHT-C is somewhat faster than that for RossThickHT-M but still much slower than
373 that for RossThickHT-X. The computation time goes roughly as the third power of the number of
374 streams. Since the number of terms used in our hotspot model is more than 10 times less than that
375 specified for the original hotspot model (as shown in the Table 1), there would be a considerable
376 performance gain with the BRDF simulations.

377

378 **Table 1.** Values of N_{BRDF} and $N_{FOURIER}$ needed to reconstruct a hotspot with $\zeta_0 = 1.5^\circ$.

		RossThickHT-M		RossThickHT-X		RossThickHT-C	
#	Accuracy (%)	NBRDF	N_FOURIER	NBRDF	N_FOURIER	NBRDF	N_FOURIER
1	1	2810	1402	278	139	1578	789
2	0.5	5620	2807	324	162	3158	1579
3	0.4	7020	3509	338	169	3948	1974
4	0.3	9360	4679	356	178	5264	2632
4	0.2	14040	7019	382	191	7896	3948
5	0.1	28080	14039	428	214	15794	7897

379 While both numbers are necessary for the reconstructed BRDF accuracy, the main impact comes
380 from the number of Fourier terms $N_{FOURIER}$ used, when the value of N_{BRDF} is twice (or more) that
381 of $N_{FOURIER}$. In Figure 2, using a fixed value $N_{BRDF} = 100$ for the RossThickHT-M, RossThickHT-
382 C and RossThickHT-X models, we show the dependence of the relative error of the reconstructed
383 BRDF on the solar zenith angle for four different values of $N_{FOURIER}$. Choices of $N_{FOURIER}$ (23, 31,
384 63 and 95) correspond to values 12, 16, 32 and 48 for the number $N_{STREAMS}$ (number of half-space
385 polar discrete ordinates) used in VLIDORT ($N_{FOURIER} = 2N_{STREAMS} - 1$). In this example, also used
386 by [Lorente et al., 2018] (their Figure 6), the BRDF represents a vegetated surface over Amazonia
387 at wavelength 758 nm with free parameters $[P_1, P_2, P_3] = [0.36, 0.24, 0.03]$ taken from MODIS
388 band 2 (841–876 nm) to account for the increase in surface reflectivity near 700 nm.

389 Overall, the error decreases with increasing values of $N_{FOURIER}$. The error also increases with those

Formatted: Font: 12 pt, Not Bold, Not Italic

Formatted: Font: 12 pt, Not Bold, Not Italic

Formatted: Font: Not Bold

Formatted: Font: Not Bold, Not Italic

Formatted: Font: Not Bold

Formatted: Font: Not Bold, Not Italic

Formatted: Font: Not Bold

Formatted: Font: Not Bold, Not Italic

Formatted: Font: Not Bold

Formatted: Font: Not Bold, Not Italic

Formatted: Font: Not Bold

Formatted: Font: Not Bold, Not Italic

Formatted: Font: Not Bold

Formatted: Font: Not Bold, Not Italic

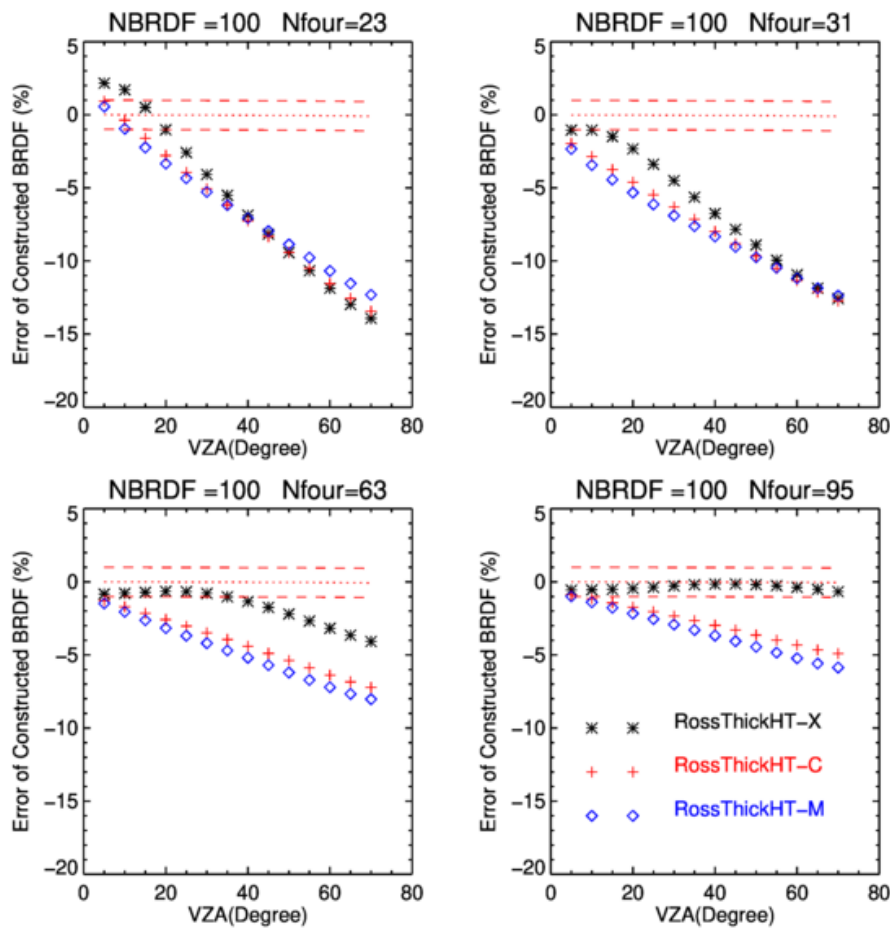
Formatted: Font: Not Bold

Formatted: Font: Not Bold, Not Italic

Formatted: Font: Not Bold

390 viewing angles at which the hotspot occurs, since the hotspot peaks are higher and narrower for
 391 larger viewing angles. Errors for all three models are large when N_{FOURIER} is as small as 23. The
 392 advantage of RossThickHT-X starts to show when N_{FOURIER} increases to 31, but this is not
 393 significant when the hotspot viewing angle is larger than 45° . When N_{FOURIER} is set to 95, the
 394 performance of RossThickHT-X is much better than that for the other two models; the error is less
 395 than 1% even for large viewing hotspot angles, whereas the corresponding errors using
 396 RossThickHT-M or RossThickHT-C are still at the 5-8% level for hotspots at viewing angles
 397 larger than 30° . Overall, the error with RossThickHT-C is slightly smaller than that for
 398 RossThickHT-M.

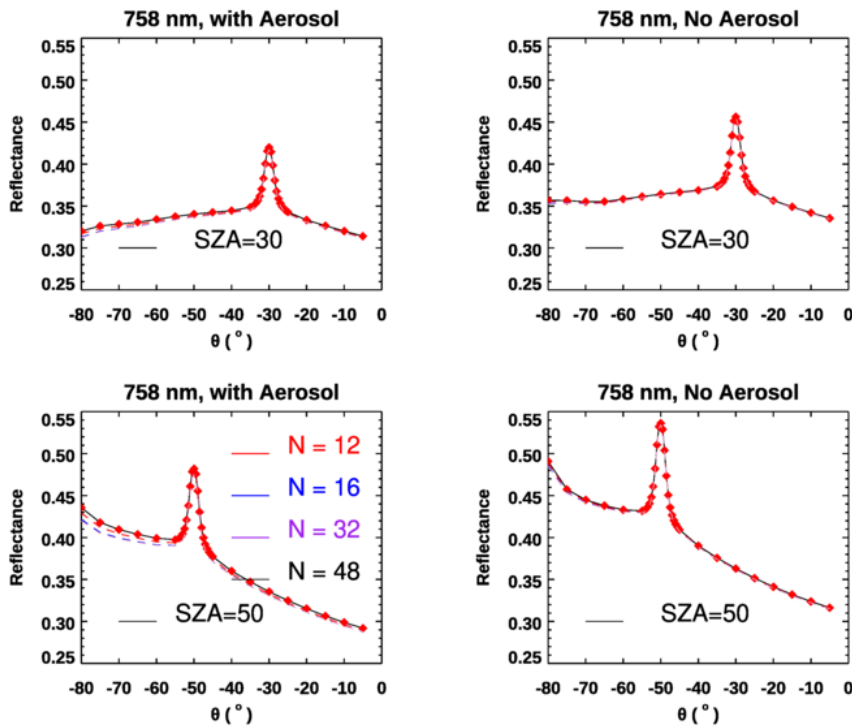
399



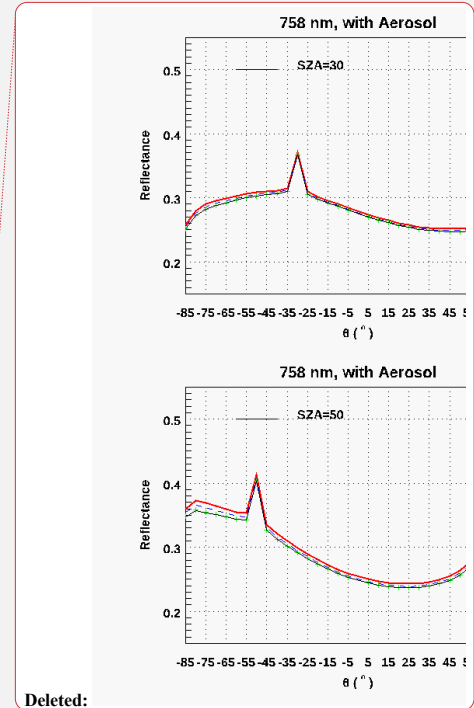
400

401 **Figure 2.** Accuracy of Fourier-reconstructed BRDFs relative to their exact values, for the three
 402 Ross-Li models. $N_{BRDF} = 100$, with $N_{FOURIER}$ set to four different values as indicated. Surface
 403 BRDF parameters represent a vegetated surface over Amazonia at 758 nm, with $[P_1, P_2, P_3] =$
 404 $[0.36, 0.24, 0.03]$.

405 Next we examine simulated TOA reflectances at 758 nm with the three hotspot models providing
 406 inputs to the main VLIDORT RT calculations. We again set $N_{BRDF} = 100$ and $N_{STREAMS} = 12, 16, 32$
 407 and 48. Results are shown in Figure 3 for two solar zenith angles. The hotspot signature is evident
 408 at 30° (upper panels) and 50° (lower panels), and the peak signature with aerosols present is higher
 409 than that without aerosol. The widths of the hotspots in Figure 3 are very similar, confirming the
 410 argument of [Powers and Gerstl, 1988] that the hotspot width is expected to be relatively invariant
 411 to atmospheric perturbations. Lines of different colors correspond to simulations using different
 412 values of $N_{STREAMS}$; in general, differences between these lines are pretty small, especially in the
 413 atmosphere without aerosol and when the viewing angle is less than 60° . To better illustrate
 414 patterns in TOA reflectance values using different values $N_{STREAMS}$, we used the simulated
 415 reflectances obtained with $N_{STREAMS} = 48$ as the reference, and the results of this comparison are
 416 shown in Figure 4.



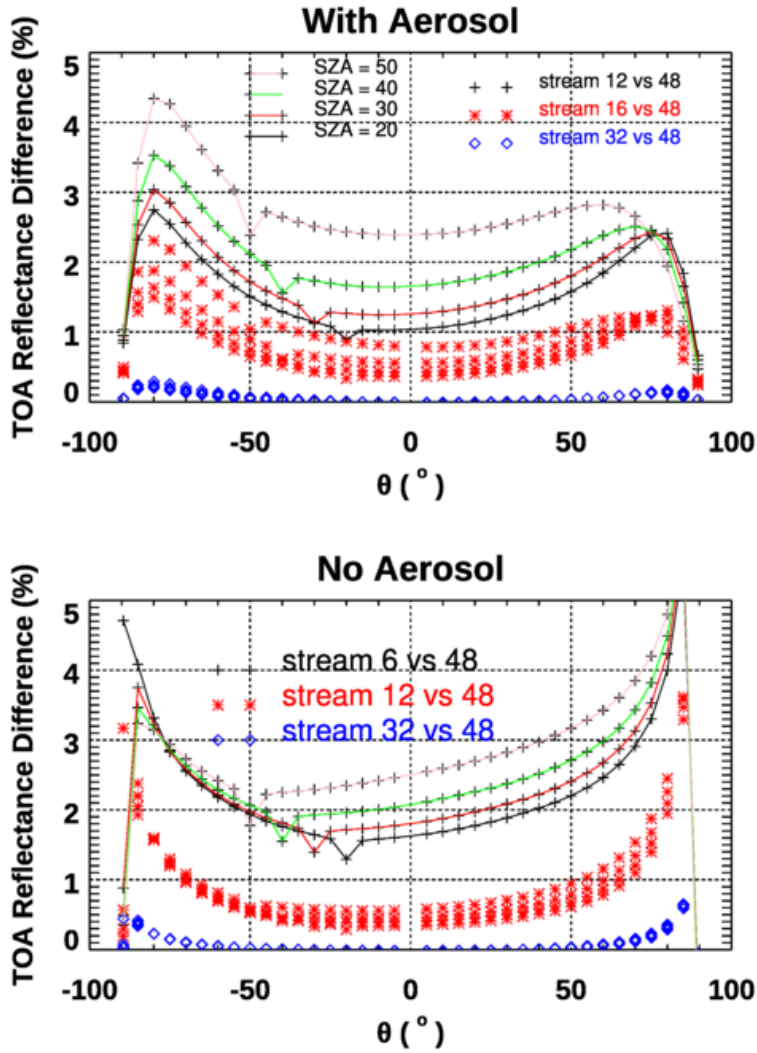
417
 418 **Figure 3.** TOA reflectance as a function of viewing zenith angle, simulated by VLIDORT at 758
 419 nm with a Ross-Li surface BRDF model with hotspot correction RossThickHT-X. Geometries



Deleted:

421 are in the principal plane for two solar zenith angles as indicated, and results were obtained with
 422 and without aerosol. Surface BRDF parameters represent a vegetated surface over Amazonia at
 423 758 nm with $(P_1, P_2, P_3) = (0.36, 0.24, 0.03)$. The red solid line represents the simulation N_{STREAMS}
 424 = 12, blue dashed line is for $N_{\text{STREAMS}} = 16$, with the remaining lines for $N_{\text{STREAMS}} = 32$ (green)
 425 and $N_{\text{STREAMS}} = 48$ (dark); the latter two lines are almost aligned.

Formatted: Strikethrough



426
 427

428 **Figure 4.** Same set-ups as Figure 3, but now plotting the TOA reflectance differences with four
429 solar zenith angles as indicated.

430 From Figure 4 it is evident that relative differences in TOA reflectances for an atmosphere with
431 aerosols are larger than those for the atmosphere without aerosols. As the typical viewing angle
432 range for BRDF kernels is mostly within 60° , we will focus on these differences for viewing angles
433 $< 60^\circ$. In the upper panel we see that TOA differences (comparing $N_{\text{STREAMS}} = 12$ with N_{STREAMS}
434 $= 48$) increase with solar zenith angle; the difference at $\text{SZA} = 50^\circ$ is almost double than that at
435 $\text{SZA} = 20^\circ$. The relative difference in percentage at the hotspot region is smaller than beyond
436 hotspot, which is easy to understand as the absolute value of the TOA reflectance at the hotspot is
437 larger. In both cases with and without aerosol, TOA reflectance differences (comparing N_{STREAMS}
438 $= 32$ with $N_{\text{STREAMS}} = 48$) are very small; VLIDORT simulations with $N_{\text{STREAMS}} = 32$ are accurate
439 enough in this case.

440 For the atmosphere with aerosol, the bias in simulated TOA reflectances using $N_{\text{STREAMS}} = 16$
441 (relative to $N_{\text{STREAMS}} = 48$) is 0.5-1.0%. In the clear atmosphere without aerosol, the bias of using
442 $N_{\text{STREAMS}} = 6$ can be in the region 2-3%, but the bias with $N_{\text{STREAMS}} = 12$ is around 0.5%,
443 suggesting that the setting for N_{STREAMS} should be 12 or higher in a Rayleigh atmosphere overlying
444 a hotspot surface.

445 As noted already, $N_{\text{FOURIER}} = 2N_{\text{STREAMS}} - 1$. Compared to the value of N_{FOURIER} needed for
446 reconstruction of surface BRDFs near the hotspot (Table 1), that is, $N_{\text{FOURIER}} = 139-162$ for an
447 accuracy of 0.5-1.0%, the values of $N_{\text{FOURIER}} = 23$ (for the Rayleigh scenario) and $N_{\text{FOURIER}} = 63$
448 (for the atmosphere with aerosol) needed for full VLIDORT RT simulations are much smaller.
449 The reason for this reduction lies with the separation in VLIDORT between the first order (FO:
450 single scattering and direct reflectance) calculations and the multiple-scatter (MS) calculations in
451 VLIDORT. The first-order calculation in VLIDORT is always done with full accuracy with solar
452 beam and line-of-sight attenuations treated for a curved atmosphere, and with an exact value for
453 the surface BRDF used to calculate the “direct-bounce” reflectance (which is very often the
454 dominant contribution from the surface). No Fourier reconstruction is necessary for this
455 contribution. For the MS contribution, multiple scatter is treated using Fourier cosine/sine azimuth
456 expansions and associated Fourier terms for both the truncated phase matrix for scattering and the
457 diffuse-field BRDF contributions. The important point to note here is the use of the exact BRDF
458 for the direct-bounce contribution in VLIDORT; RT models without this FO/MS separation will
459 be constrained by the need to use a Fourier-expanded reconstruction for the direct-bounce BRDF
460 contribution.

461 The results shown in Figures 3-4 are confined to a single standard atmosphere and aerosol model.
462 In the next section below, we use VLIDORT simulations to investigate the impact of scattering on
463 hotspot signatures. For this study, we choose $N_{\text{BRDF}} = 200$ and $N_{\text{STREAMS}} = 32$; this should be
464 conservative enough to avoid any uncertainty associated with the use of surface BRDFs and the
465 choice of stream numbers in VLIDORT.

466 *3.2. Impact of scattering on the hotspot signature at TOA*

467 Here we use the three parameters $(P_1, P_2, P_3) = (0.0399, 0.0245, 0.0072)$ for the RTLSR surface
468 BRDF model. These are the spatially averaged parameters from MODIS (BRDF/albedo product
469 MCD43A1) band 3 (459–479 nm) over Amazonia (latitude $5^\circ \text{N} - 10^\circ \text{S}$, longitude $60 - 70^\circ \text{W}$)
470 for March 2008 [Lorente et al., 2018]. TOA reflectances are calculated as a function of viewing

471 zenith angle in the principal plane, with the solar zenith angle set at 30° (Figure 5). In this
 472 experiment, ~~we simulated two atmospheric conditions with and without aerosol and~~ using the
 473 new hotspot correction model, RossThickHT-X, and ~~the~~ RTLSR BRDF model without a hotspot
 474 correction (RossThick). ~~From the comparison of TOA reflectances at all angles between the left~~
 475 ~~and the right panels in Figure 5, we can see that the TOA reflectance in the atmosphere with~~
 476 ~~aerosol is overall larger than that without aerosol, indication the aerosol scattering increases the~~
 477 ~~TOA reflectance. Compared to the molecular scattering only, the addition of aerosol leads to an~~
 478 ~~increase of TOA reflectance near hot spot peak by ~ 8% and 17% at 469 and 645 nm~~
 479 ~~respectively. However, from a comparison of the TOA reflectances with and without hotspot~~
 480 ~~correction, i.e. using RossThickHT-X and RossThick, we found that at 469 nm the increase of~~
 481 ~~surface reflectance at hot spot results in an increase of TOA reflectance by ~ 4% for atmosphere~~
 482 ~~with molecular scattering only, while in the atmosphere with moderate aerosol the value of~~
 483 ~~increase is only 2%. At 645 nm, the values of reflectance increase at hot spot are about 12.5%~~
 484 ~~and 7% for atmosphere with and without aerosol, indicating that for the longer wavelength at 645~~
 485 ~~nm, the TOA-hotspot signature is much stronger than at 469 nm. The smaller TOA-hotspot~~
 486 ~~signature at 469 nm is due to the influence of stronger Rayleigh scattering. The inclusion of~~
 487 ~~aerosol scattering smooths out the hotspot signature at the TOA by ~44% to -50% compared to~~
 488 ~~the atmosphere with molecular scattering only in these two wavelengths, suggesting aerosol~~
 489 ~~scattering further smooths out the hotspot signature at the TOA, and makes it harder to~~
 490 ~~discriminate the TOA reflectance difference between the runs with and without hotspot~~
 491 ~~correction. This observation agrees with the results from [Bréon et al., 2002], in which it was~~
 492 ~~noted that no significant hotspot signature has been observed when the surface reflectance is very~~
 493 ~~small, as in the blue channel or over the ocean.~~

Deleted: two calculations are plotted, one

Deleted: the other using

Formatted: Font: Not Italic

Formatted: Font: Not Italic

Formatted: Font: Not Italic

Formatted: Font: Not Italic

Formatted: Font: Not Italic

Formatted: Font: Not Italic

Formatted: Font: Not Italic

Formatted: Font: Not Italic

Deleted: From Figure 5 it is clear that the

Deleted: very small, likely

Deleted: T

Deleted: he addition of

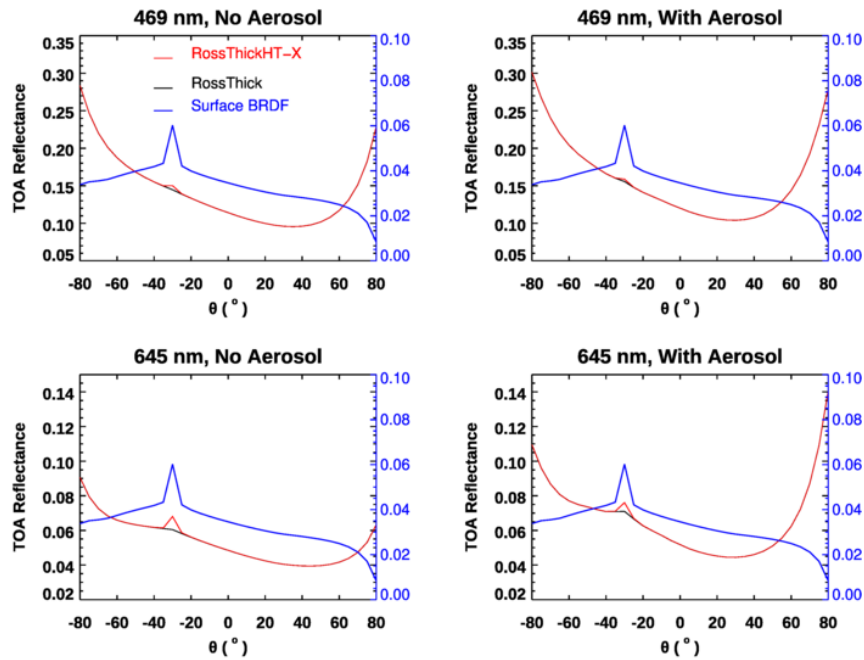
Deleted: reduces

Deleted: SZA 30°

Deleted: is

Deleted: For the longer wavelength at 645 nm, the TOA-hotspot signature is obvious, and the addition of aerosol scattering reduces the hotspot signature slightly compared to the situation with molecular scattering only.

Formatted: Font: Font color: Auto



507
508

509 **Figure 5.** VLIDORT TOA reflectances as a function of viewing zenith angle with solar angle 30° in
 510 the principal plane, at 469 and 645 nm using a Ross-Li surface BRDF model **RossThick** and
 511 **RossThickHT-X**, and with and without aerosol. The aerosol model used is the same as in Figure 3,
 512 with optical depth 0.2. Surface BRDF parameters represent a vegetated surface over Amazonia with
 513 $(P_1, P_2, P_3) = (0.0399, 0.0245, 0.0072)$, and blue curves are surface reflectance.

514 We also examine the hotspot signatures in 765 and 865 nm, two wavelengths used in POLDER
 515 data analysis. The three linear weighting parameters in the BRDF model are $(P_1, P_2, P_3) = (0.36,$
 516 $0.24, 0.03)$, which is the same set as that used by [Lorente et al., 2018]. As noted already, these
 517 are taken from MODIS band 2 (841–876 nm) to account for the “red-edge” increase in surface
 518 reflectivity near 700 nm (e.g. [Tilstra et al., 2017]). To test the representativeness of band 2 at 758
 519 nm, Lorente et al.[2018] scaled the parameters from band 3 (459–479 nm) using the ratio of
 520 reflectances at 772 nm and 469 nm; they found that differences with parameters taken from
 521 MODIS band 2 were negligible. Since we would like to focus on the difference of the impact of
 522 atmospheric scattering on the hotspot signatures at 758 and 865 nm, we have chosen to use the
 523 same two sets of surface BRDF parameters. The results are plotted in Figures 6 and 7. To highlight
 524 the differences caused by the $3\pi/4$ factor normalizing the volume-scattering kernels K_{vol} (see note
 525 in Section 2.2), we have added in Figure 7 two simulated TOA reflectances, one based on the
 526 original hotspot correction model from Maignan et al. [2004] (RossThickHT-M) and the other
 527 using the BRDF noted in the paper of Lorente et al. [2018] (indicated by “RossThickHT-L”).
 528 Compared to Figure 5, much larger TOA-hotspot signatures at both 865 and 758 nm are evident

Deleted: ¶

Deleted: with hotspot correction

Deleted:

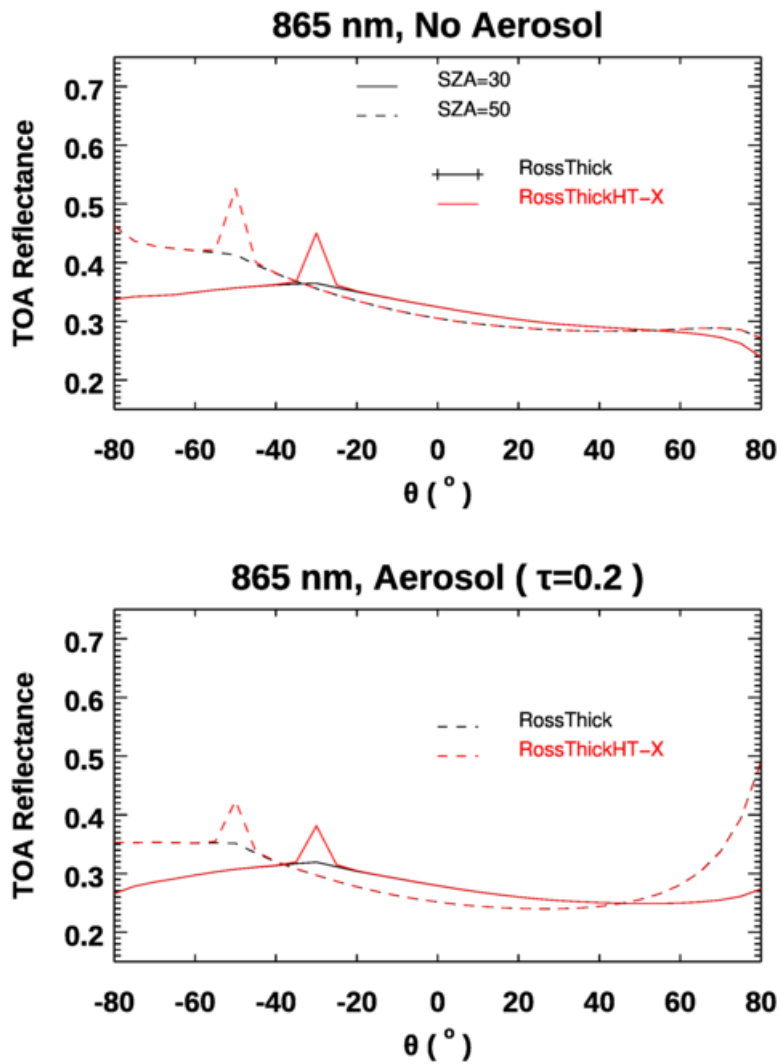
Deleted: .

Deleted: .

534 in Figures 6 and 7 respectively, and they are slightly larger at SZA=50° than at SZA=30°. As
535 expected, in the scattering region within 2° of hot spot there are some differences between
536 RossThickHT-M and RossThickHT-X, but beyond the hotspot ($\pm 5^\circ$), the TOA reflectance using
537 RossThickHT-X agrees very well with that using the original RossThick model. However, from
538 Figure 7, we see that the simulated reflectance using RossThickHT-M is slightly larger than that
539 using RossThick model even in a region of $\pm 15^\circ$ beyond the hotspot, particularly in the large
540 viewing angles in the forward direction. In the region of $\pm 5^\circ$ to $\pm 15^\circ$ beyond the hotspot, the
541 simulated reflectance using RossThickHT-M is clearly larger than that using RossThick and
542 RossThickHT-X.

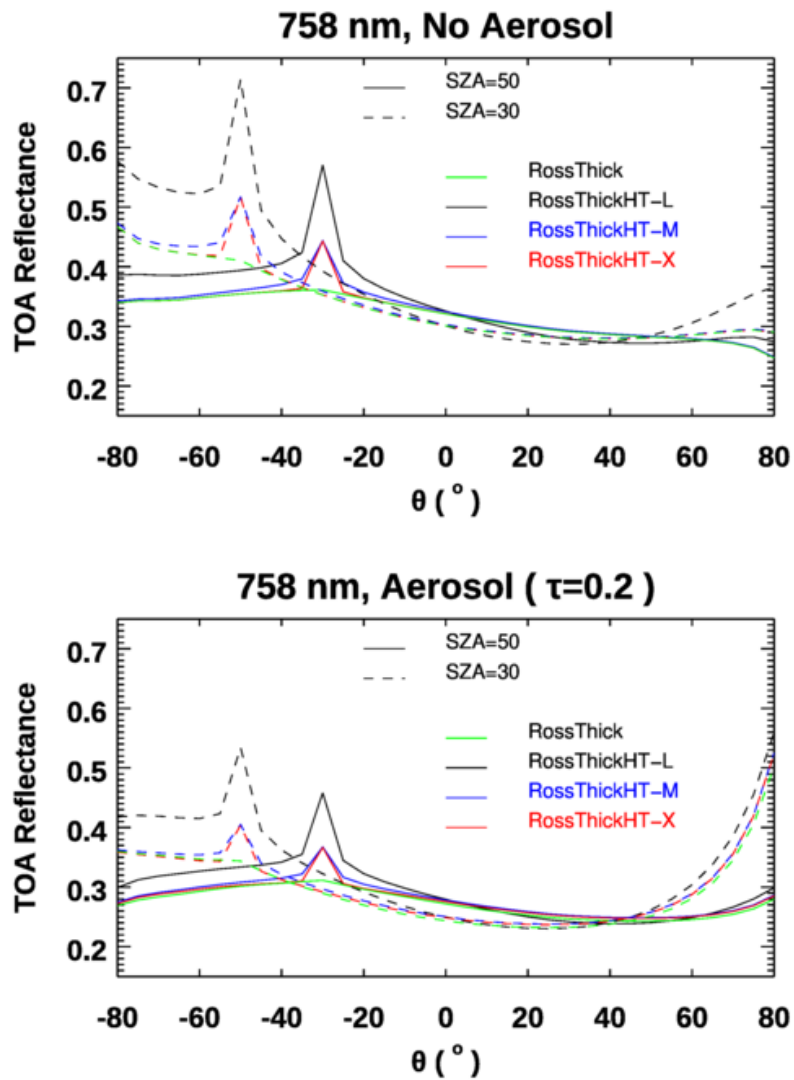
543

Formatted: Superscript



544
545
546
547

Figure 6. Same as Figure 5 but results are calculated at 865 nm for solar zenith angles 30° and 50°. Surface BRDF parameters represent a vegetated surface over Amazonia with $(P_1, P_2, P_3) = (0.36, 0.24, 0.03)$.



548

549 **Figure 7.** Similar to Figure 6 but results calculated at wavelength 758 nm. For comparison, we
 550 have added simulated TOA reflectances using the original hotspot correction model from
 551 [Maignan et al., 2004] (RossThickHT-M) and again using the model in [Lorente et al., 2018],
 552 which is a factor of $4\pi/3$ times larger than RossThickHT-M in the hotspot region and is denoted
 553 here as RossThickHT-L.

554 To better quantify the hotspot effect and the impact due to scattering in the atmosphere, we define
555 the “hotspot amplitude” as the difference between the TOA reflectance at the hotspot and the
556 corresponding TOA reflectance calculated without hotspot correction, namely:

557
$$HT_{Amplitude} = \frac{R(\theta_0, \theta, \varphi = 180, RossThickHT - Li)}{R(\theta_0, \theta, \varphi = 180, RossThick - Li)}$$

558 The impacts of molecular and aerosol scattering on these amplitudes are illustrated in Figure 8 for
559 a range of hotspot viewing angles and for four wavelengths. For comparison, the hotspot
560 amplitudes at the surface are also plotted. From Figure 8, it is evident that scattering in the
561 atmosphere smooths out the hotspot signature at TOA, and the impact of scattering is much larger
562 in the visible compare with that in the near-infrared part of the spectrum. Even in the visible, the
563 amplitude of the hotspot signature at 469 nm is much smaller than that at 645 nm. ~~When the SZA
564 increases from 20° to 50°, the HS amplitude at 469 nm decreases by -1.34% and -1.08% for
565 atmospheric conditions without aerosol and with aerosol, respectively. The HS amplitude at 645
566 nm decreases by -1.24% and -2.14% similarly. In contrast, the HS amplitudes increase by 3.36
567 (0.03)% at 758 nm, and by 3.9 (1.5) % at 865 nm as SZA increases from 20° to 50°. Since
568 molecular scattering is much smaller than in the visible, the large difference in the amounts of HS
569 amplitude increase between no-aerosol and with-aerosol conditions indicates the impact of
570 multiple scattering, and the existence of aerosol smooths out the TOA hotspot signature. The
571 increase of HS amplitudes with SZA following with the increase of surface reflectance in the near
572 infrared, particularly in the no-aerosol condition, indicates that the HS amplitude is largely affected
573 by surface reflectance in the near infrared.~~

574 These simulated results agree well with the analysis of POLDER data by [Bréon et al.,
575 2002]; at 440 nm, they found that the amplitude of the hotspot signature is very small. The much
576 larger amplitudes observed at 758 nm and 865 nm also confirm the findings by [Maignan et al.,
577 2004], who showed that near-infrared measurements are preferred to those in the visible, not only
578 because of the larger-amplitude directional effects but also because of the lower atmospheric
579 perturbation. Indeed, Maignan et al.[2004] suggested that near-infrared measurement data is better
580 suited for the evaluation of different BRDF models. ~~From Figure 8 we can also see that in the near-
581 infrared, the amplitude of the hotspot signature increases with the zenith angle (right panel);
582 however, the angular dependencies in the surface hotspot and the TOA hotspot are almost opposite
583 in the visible, especially for an atmosphere without aerosols.~~

Formatted: Justified

Formatted: Superscript

Formatted: Font: Not Italic

Formatted: Font: Not Italic

Formatted: Font: Not Italic

Formatted: Font: Not Bold, Not Italic

Formatted: Font: Not Bold

Formatted: Font: Not Bold, Not Italic

Formatted: Font: Not Bold, Not Italic

Formatted: Font: Not Bold, Not Italic

Formatted: Font: Not Bold, Not Italic

Deleted: Similarly, the amplitude in 758 nm is smaller than that at 865nm.

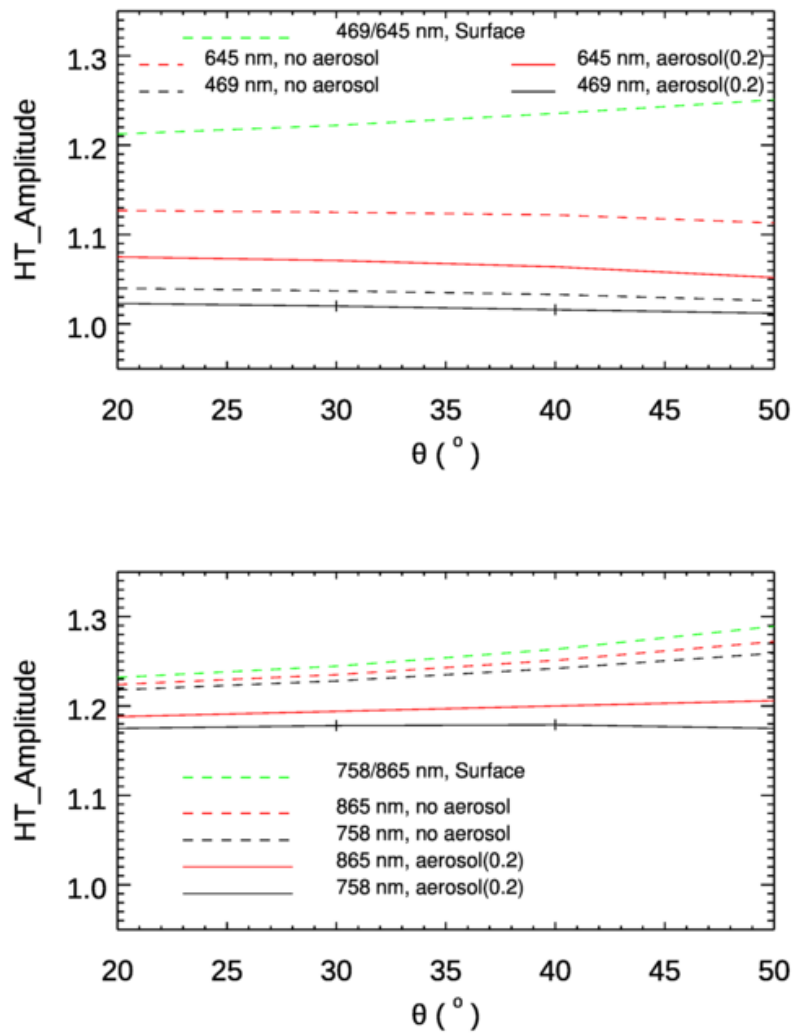
Formatted: Font: Not Bold, Not Italic

Formatted: Font: Not Italic

Formatted: Indent: First line: 0.5"

Deleted: , confirming that the atmospheric contribution to the reflectance increase at the backscattering direction is negligible

Formatted: Strikethrough



589

590 **Figure 8.** Comparison of hotspot amplitudes at the TOA for an atmosphere with and without
 591 aerosols in visible (469 and 645 nm, left panel) and near-infrared (658 and 865 nm, right panel).
 592 Hotspot amplitudes at the surface are computed using the differences between the RossThickHT-
 593 Li and RossThick-Li BRDF models.

594 In the processing of POLDER data done by [Bréon et al., 2002] and [Maignan et al., 2004], only
595 molecular scattering to first order was taken into account for the atmospheric correction. As there
596 is no correction for the effects of aerosol scattering or the coupling of surface reflectance with
597 molecular scattering, absolute values of the reflectances may not be fully representative of the
598 surface for POLDER [Bréon et al., 2002]. From our simulations shown in Figure 8, the amplitude
599 of the hotspot signature with aerosol scattering included is smaller than that without aerosol,
600 suggesting that the results from POLDER [Bréon et al., 2002] might underestimate the amplitude
601 of hotspot signature at the surface. Based on the differences of the HS amplitudes between the
602 atmosphere with aerosol and without aerosol, we estimate that, on average, the HS amplitude is
603 underestimated by 4.0 ± 1.7% when not considering aerosol for a moderately polluted atmosphere
604 with optical depth of 0.2, even though most satellite observations are less affected by the aerosols
605 than this simulation may suggest.

606
607 A final issue is related to a factor difference that exists between the equation of [Lorente et al.,
608 2018] (i.e. their Eq. A1) with our Eq. (8), which is the one used in [Maignan et al., 2004]. The one
609 used by [Lorente et al., 2018] is $3\pi/4$ times larger; this discrepancy results in a TOA-hotspot
610 signature more than twice as large, as shown in Figure 7. Since we used the same BRDF parameters
611 as [Lorente et al., 2018], this factor difference is the main reason that the TOA-hotspot signatures
612 shown by [Lorente et al., 2018] (their Figure 5) at 469 and 645 nm from their DAK model are
613 higher than our simulated results in this paper. In addition, in the paper of Lorente et al., 2018, the
614 authors obtained the VLIDORT result using an older version of the code, and this result showed
615 the hotspot peak that was smaller than that generated with the other RT models. We think the
616 reason for this lies with a scaling factor difference between the hotspot BRDF equation cited in
617 [Lorente et al., 2018] and the equation used in the earlier VLIDORT model. Hence, we have added
618 this simulation result here in order to bring attention to users when using scaling factor data from
619 the MODIS BRDF product. From the upper panel of Figure 7, it is evident that the hotspot peak
620 using RossThickHT-L seems too high, particularly for the hotspot occurring at 50°. From the
621 analysis of POLDER data, Bréon et al.[2002] found that the hotspot reflectance amplitude is
622 generally of the order 0.10–0.20 at 865 nm and 0.03–0.18 at 670 nm, although the full range of
623 values is wide. Therefore, we think that the use of an equation with a factor of $3\pi/4$ discrepancy is
624 likely to overestimate the hotspot effect, and we caution users to be careful to check the equations
625 for the presence of this $3\pi/4$ factor, particularly when using MODIS BRDF products.

Formatted: Font: Not Bold, Not Italic

Formatted: Font: Not Bold, Not Italic

Formatted: Font: Not Bold, Not Italic

Formatted: Font: Not Bold, Not Italic

Formatted: Font: Not Bold, Not Italic

Deleted: T

Deleted: the ones

Deleted: observed

Formatted: Font: Not Bold, Not Italic

Formatted: Font: Not Bold, Not Italic

Formatted: Font: Not Bold, Not Italic

Deleted: as seen in [Lorente et al., 2018] (their Figure 5), the lower TOA-hotspot signature generated by LIDORT (as opposed to those from the other two RTMs) is likely due to the deployment of an older version of LIDORT that did not include the hotspot correction

Formatted: Strikethrough

Formatted: Strikethrough

Formatted: Strikethrough

Formatted: Strikethrough

Formatted: Strikethrough

Formatted: Strikethrough

Deleted: even

635 **4. Summary and Conclusions**

636 In remote sensing, it is common practice to deploy a simple kernel-driven semi-empirical model
637 with three free parameters to represent land surface BRDFs (excepting snow and ice); the
638 commonly used model is the RossThick/LiSparse combination with a correction to account for the
639 hotspot [Maignan et al., 2004]. In our study, we modified this BRDF model to improve
640 convergence of the Fourier azimuth series decomposition. Furthermore, using this new hotspot
641 model, we studied the impact of Rayleigh scattering and aerosol on the TOA atmospheric hotspot
642 signature in the visible and near-infrared wavelengths using the VLIDORT RTM.

643 With the improved hotspot correction, we found that the numbers of Gaussian points (N_{BRDF}) and
644 Fourier Terms ($N_{FOURIER}$) are more than 10 times smaller than those needed with the original
645 hotspot model from Maignan et al. [2004]; this makes our BRDF model much more practical for
646 use with VLIDORT to simulate the hotspot signature at the TOA. Another advantage of this
647 modified model is that the new hotspot model agrees very well with the original RossThick model
648 away the hotspot region, thus allowing the use of this single model in the conditions with and
649 without hotspot in applications.

650 We carried out a number of investigations on the impact of molecular and aerosol scattering on
651 the hotspot signature at the TOA. TOA reflectances were calculated for different solar and viewing
652 angles and at four wavelengths. These simulations using VLIDORT show that:

- 653 1. In agreement with previous analysis using POLDER measurement data, hotspot signatures
654 in the near-infrared are larger than those in the visible as it is less impacted by molecules
655 scattering, making it better to be used to derive the surface hotspot signature.
- 656 2. Also in agreement with the POLDER study, the hotspot amplitudes at TOA and the surface
657 both increase with solar zenith angle in the near-infrared; however, at 469 and 645 nm, this
658 increase with solar zenith angle is not obvious at TOA, due to stronger Rayleigh scattering
659 at shorter wavelengths, which is more pronounced for longer path lengths at larger solar
660 zenith angles.
- 661 3. Scattering by molecules and aerosols in the atmosphere tends to smooth out the hotspot
662 signature at TOA, and the hotspot amplitude is reduced when aerosols are added to an
663 otherwise clear (Rayleigh scattering only) atmosphere. ~~These results also showed that~~
664 ~~atmospheric scattering does not generate hotspot-like signatures and does not change the~~
665 ~~width of the BRDF-induced hotspot.~~
- 666 4. In VLIDORT, the direct-beam solar reflectance is calculated using the exact BRDF (rather
667 than in a truncated Fourier-series form); this means that smaller values of $N_{FOURIER}$ (i.e. 23
668 and 63 for atmospheres without and with aerosol scattering) can be used in for the multiple
669 scattering calculations in VLIDORT to obtain hotspot signature with acceptable accuracy.

670 Since atmospheric corrections in the POLDER data processing were performed using Rayleigh-
671 only single scattering without any consideration of aerosol, from our simulations we found that
672 the amplitude of hotspot signature at the surface is likely underestimated by 4.0 ± 1.7% in the
673 analysis of hotspot signature using POLDER data [Bréon et al., 2002], highlighting the importance
674 to consider the multiple scattering and to include aerosols in the retrievals of surface BRDF
675 (hotspot).

676 Another issue related to the hotspot correction in the model used by Lorente et al. [2018] is the
677 scaling by a factor of 3π/4; this may lead to the amplitude of hotspot too high in large solar zenith

Deleted: best

Deleted: and

Deleted: correction

Deleted: further

Deleted: We also showed

Deleted: .

Deleted: ; the main findings from our study are

Deleted: .

Deleted: .

Formatted: Font: (Default) Times New Roman

Formatted: Font: (Default) Times New Roman

Formatted: Font: (Default) Times New Roman

Formatted: Strikethrough

Deleted: A

Deleted: . O

Deleted: suggest

Deleted: .

Formatted: Strikethrough

Formatted: Strikethrough

Formatted: Strikethrough

691 angle. It is recommended that users take care to check the kernel equations when using the three
692 parameters from MODIS BRDF products to generate the BRDF.

693 ~~The agreement between our simulated results and observations from POLDER measurements
694 enhances our understanding of the nature of the hotspot and the impact on it by atmospheric
695 scattering. It is also clear that VLIDORT makes accurate simulations of the hotspot effect, and the
696 results obtained here can be used as benchmarks. Our improved hotspot kernel is now a standard
697 feature in the latest version of the VLIDORT BRDF supplement code that significantly improve
698 the numerical efficiency. Since this new model has not been validated using any real observation
699 data, and considering the difference between this model and the original hotspot model from
700 Maignan et al. [2004] in scattering angles close to the peak of hotspot, it may not be appropriate
701 for those who need an exact representation of the hot spot angular signature around the peak of
702 hotspot.~~

703

704 **Description of author's responsibilities**

705 XX, XL and RS conceived of the idea. XX and RS led the writing. All authors edited the
706 manuscript.

707 **Funding**

708 This research was supported by NASA SBG program.

709 **CRediT authorship contribution statement**

710 **Xiaozhen Xiong:** Methodology, Writing – original draft, Formal analysis, Investigation. **Xu**
711 **Liu:** Funding acquisition, Supervision, Writing – review & editing, Conceptualization. **Robert**
712 **Spurr:** Methodology, Writing – review & editing, Formal analysis. **Ming Zhao:** Coding,
713 Analysis. **Wan Wu, Qiguang Yang, Liqiao Lei:** Writing – review & editing.

714 **Declaration of Competing Interest**

715 The authors declare that they have no known competing financial interests or personal
716 relationships that could have appeared to influence the work reported in this paper.

717 **Acknowledgements**

718 This research was supported by the NASA SBG program and JPL. Resources supporting
719 this work were provided by the NASA High-End Computing (HEC) Program through the NASA
720 Advanced Supercomputing (NAS) Division at NASA Ames Research Center.
721

Deleted: Our results highlight the importance of the including aerosol scattering in the retrievals of surface BRDF (hotspot).

Formatted: Strikethrough

Formatted: Justified, Space Before: 0 pt, No bullets or numbering, Don't adjust space between Latin and Asian text, Don't adjust space between Asian text and numbers

Deleted: ¶

Formatted: Font: (Default) Times New Roman, 12 pt

Formatted: Font: (Default) Times New Roman, 12 pt

Formatted: Font: (Default) Times New Roman, 12 pt

Formatted: Font: (Default) Times New Roman, 12 pt

Formatted: Subscript

726 **References**

- 727 Bacour, C., and F.-M. Bréon. Variability of biome reflectance directional signatures as seen by
728 POLDER, *Remote Sens. Environ.*, **98**(1), 80-95, <https://doi.org/10.1016/j.rse.2005.06.008>, 2005.
- 729 Baldridge, A.M., S. J. Hook; C. I. Grove, and G. Rivera. The ASTER spectral library version 2.0.
730 *Remote Sens. Environ.*, **113**, 711–715, 2000.
- 731 Bicheron, P. and M. Leroy. Bidirectional reflectance distribution function signatures of major
732 biomes observed from space. *Journal of Geophysical Research*, **105**, 26669-26681,
733 <https://doi.org/10.1029/2000JD900380>, 2002.
- 734 Bréon, F.M., F. Maignan, M. Leroy, and I. Grant. Analysis of hotspot directional signatures
735 measured from space. *Journal of Geophysical Research*, **107**, 4282-4296, 2002.
- 736 Chen, J. M., and S. G. Leblanc. A four-scale bidirectional reflectance model based on canopy
737 architecture. *IEEE Transactions on Geoscience and Remote Sensing*, **35**,1316-1337 (1997).
- 738 Chen, J. M., and J. Cihlar. A hotspot function in a simple bidirectional reflectance model for
739 satellite applications. *Journal of Geophysical Research*, **102**, 25907-25913 (1997).
- 740 de Rooij, W. A., and C. C. A. H. van der Stap. Expansion of Mie scattering matrices in generalized
741 spherical functions. *Astron. Astrophys.*, **131**, 237-248, 1984.
- 742 de Haan, J. F., P. B. Bosma, and J. W. Hovenier. The adding method for multiple scattering of
743 polarized light. *Astron. Astrophys.*, **183**, 371-391, 1987.
- 744 Deschamps, P.Y., F.M. Bréon, M. Leroy, A. Podaire, A. Bricaud, J.C. Buriez, G. Sèze. The
745 POLDER mission: Instrument characteristics and scientific objectives. *IEEE Transactions on*
746 *Geoscience and Remote Sensing*, **32**, 598-615, 1994.
- 747 Egbert, D.D. A practical method for correcting bidirectional reflectance variations. *Proceedings*
748 *of Symposium on Machine Processing of Remotely Sensed Data.*, **1977**, 178-188. Available online:
749 https://docs.lib.purdue.edu/cgi/viewcontent.cgi?article=1204&context=lars_symp (accessed on
750 20/03/2020)
- 751 Gao, B. C., M. J. Montes, C. O. Davis, and A. F. H. Goetz. Atmospheric correction algorithms for
752 hyperspectral remote sensing data of land and ocean. *Remote Sensing Environment*, **113**(S1), S17–
753 S24, 2009.
- 754 Godsalve, C. Bidirectional reflectance sampling by ATSR-2: A combined orbit and scan model,
755 *International Journal of Remote Sensing*, **16**, 269-300, 1995.
- 756 Gutman, G.G. The derivation of vegetation indices from AVHRR data. *International Journal of*
757 *Remote Sensing*, **8**, 1235-1243, 1987.
- 758 Hapke, B.W. Bidirectional reflectance spectroscopy: 1. Theory. *J. Geophys. Res.* **86**, 3039-3054,
759 1981.
- 760 Hapke, B.W. Bidirectional reflectance spectroscopy: 4. The extinction coefficient and the
761 opposition effect. *Icarus* **67**, 264-280, 1981.
- 762 Hess M., P. Koepke and I. Schult, Optical properties of aerosols and clouds: the software package
763 OPAC, *Bull. Am. Meteorol. Soc.*, **79**, 831-844, 10.1175/1520-
764 0477(1998)079<0831:OPOAAC>2.0.CO;2

765 Hovenier, J. W., and C. V. M. van der Mee, Fundamental relationships relevant to the transfer of
766 polarized light in a scattering atmosphere. *Astron. Astrophys.*, **128**, 1-16, 1983.

767 Jiao, Z., Y. Dong and X. Li, "An approach to improve hotspot effect for the MODIS BRDF/Albedo
768 algorithm," *2013 IEEE International Geoscience and Remote Sensing Symposium - IGARSS*,
769 Melbourne, VIC, Australia, 2013, 3037-3039, doi: 10.1109/IGARSS.2013.6723466.

770 Jupp, D. L., and A. H. Strahler, A hotspot model for leaf canopies, *Remote Sens. Environ.*, **38**,
771 193-210, 1991.

772 Kimes, D.S. Dynamics of directional reflectance factor distribution for vegetation canopies. *Appl.*
773 *Opt.*, **22**, 1364-1372, 1983.

774 Kokaly, R.F.; Clark, R.N.; Swayze, G.A.; Livo, K.E.; Hoefen, T.M.; Pearson, N.C.; Wise, R.A.;
775 Benzal, W.M.; Lowers, H.A.; Driscoll, R.L.; Klein, A.J. USGS Spectral Library Version 7: U.S.
776 Geological Survey Data Series 1035, **2017**, Available online: <https://doi.org/10.3133/ds1035>
777 (accessed on 19/03/2020).

778 Kuga, Y., and A. Ishimaru, Retroreflection from a dense distribution of spherical particles, *J. Opt.*
779 *Soc. Am.*, **A1**, 831-835, 1984.

780 Kuusk, A., The hotspot effect of a uniform vegetative cover, *Sov. J. Remote Sens.*, **3**, 645-658,
781 1985.

782 Lenoble, J., M. Herman, J. Deuzé, B. Lafrance, R. Santer, and D. Tanré. A successive order of
783 scattering code for solving the vector equation of transfer in the earth's atmosphere with aerosols,
784 *J. Quant. Spectrosc. Radiat. Transfer*, **107**, 479-507, <https://doi.org/10.1016/j.jqsrt.2007.03.010>,
785 2007.

786 Li, X. W. and A. H. Strahler. Geometric-optical bidirectional reflectance modeling of the discrete
787 crown vegetation canopy: Effect of crown shape and mutual shadowing. *IEEE Trans. Geosci.*
788 *Remote Sens.*, **30**(2), 276-292, 1992.

789 Lorente, A., F. Boersma, P. Stammes, G. Tilstra, A. Richter, H. Yu, S. Kharbouche, and J. Muller.
790 The importance of surface reflectance anisotropy for cloud and NO₂ retrievals from GOME-2 and
791 OMI. *Atmos. Meas. Tech.*, **11**, 4509-4529, <https://doi.org/10.5194/amt-11-4509-2018>, 2018.

792 Lucht, W., C. B. Schaaf, and A. H. Strahler. An algorithm for the retrieval of albedo from space
793 using semiempirical BRDF models. *IEEE Trans. Geosci. Remote Sens.* **38**, 977-998, 2000.

794 Maignan, F., F.-M Bréon, and R Lacaze. Bidirectional reflectance of Earth targets: evaluation of
795 analytical models using a large set of spaceborne measurements with emphasis on the Hotspot,
796 *Remote Sens. Environ.*, **90**(2), 210-220, <https://doi.org/10.1016/j.rse.2003.12.006>, 2004.

797 Nicodemus, F.E.; Richmond, J.C.; Hsia, J.J.; Ginsberg, I.W.; Limperis, T. Geometrical
798 considerations and nomenclature for reflectance. U.S. Department of Commerce. **1977**. Available
799 online: [https://www.gpo.gov/fdsys/pkg/GOVPUB-C13-](https://www.gpo.gov/fdsys/pkg/GOVPUB-C13-80bc81d1913dfe186083080cbdc8ae75/pdf/GOVPUB-C13-80bc81d1913dfe186083080cbdc8ae75.pdf)
800 [80bc81d1913dfe186083080cbdc8ae75/pdf/GOVPUB-C13-](https://www.gpo.gov/fdsys/pkg/GOVPUB-C13-80bc81d1913dfe186083080cbdc8ae75/pdf/GOVPUB-C13-80bc81d1913dfe186083080cbdc8ae75.pdf)
801 [80bc81d1913dfe186083080cbdc8ae75.pdf](https://www.gpo.gov/fdsys/pkg/GOVPUB-C13-80bc81d1913dfe186083080cbdc8ae75/pdf/GOVPUB-C13-80bc81d1913dfe186083080cbdc8ae75.pdf) (accessed on 20/03/2020)

802 Pinty, B. and M. Verstraete. Extracting Information on surface properties from bidirectional
803 reflectance measurements. *J. Geophys. Res.*, **96**, 2865-2874, 1991.

804 Rahman, H., B. Pinty, and M. Verstraete. Coupled Surface-Atmosphere Reflectance (CSAR)
805 Model: 2. Semiempirical Surface Model Usable With NOAA Advanced Very High Resolution
806 Radiometer Data. *J. Geophys. Res.* **98**, 20791-20801, 1998.

807 Ross, J., The radiation regime and architecture of plant stands, Dr. W. Junk Publishers, The Hague,
808 Netherlands (1981).

809 Roujean, J.-L., M. Leroy, and P.-Y. Deschamps. A Bidirectional Reflectance Model of the Earth's
810 Surface for the Correction of Remote Sensing Data. *J. Geophys. Res.*, **97**, 20455-20468 (1992).

811 Rozanov, V., A. Rozanov, A. Kokhanovsky, and J. Burrows. Radiative transfer through terrestrial
812 atmosphere and ocean: Software package SCIATRAN, *J. Quant. Spectrosc. Radiat. Transfer*,
813 **133**, 13–71, <https://doi.org/10.1016/j.jqsrt.2013.07.004>, 2014.

814 Schaaf, C.B., F. Gao, A. H. Strahler, W. Lucht, X. W. Li, T. Tsang, N. C. Strugnell, X. Y. Zhang,
815 Y. F. Jin, J. P. Muller, P. Lewis, M. Barnsley, P. Hobson, M. Disney, G. Roberts, M. Dunderdale,
816 C. Doll, R. P. d'Entremont, B. X. Hu, S. L. Liang, J. L. Privette, and D. Roy. First operational
817 BRDF, Albedo nadir reflectance products from MODIS. *Remote Sens. Environ.*, **83**(1), 135–148,
818 [https://doi.org/10.1016/S0034-4257\(02\)00091-3](https://doi.org/10.1016/S0034-4257(02)00091-3), 2002.

819 Schulz, F., K. Stamnes and F. Weng. VDISORT: An improved and generalized discrete ordinate
820 method for polarized (vector) radiative transfer, *J. Quant. Spectrosc. Radiat. Transfer*, **61**, 105-
821 122, 1999.

822 Siewert, C. E., On the equation of transfer relevant to the scattering of polarized light. *Astrophysics*
823 *J.*, **245**, 1080-1086, 1981.

824 Siewert, C. E., On the phase matrix basic to the scattering of polarized light. *Astron. Astrophys.*,
825 **109**, 195-200, 1982.

826 Siewert, C. E., A concise and accurate solution to Chandrasekhar's basic problem in radiative
827 transfer *J. Quant. Spectrosc. Radiat. Transfer*, **64**, 109-130, 2000.

828 Siewert, C. E., A discrete-ordinates solution for radiative transfer models that include polarization
829 effects. *J. Quant. Spectrosc. Radiat. Transfer*, **64**, 227-254, 2000.

830 Stamnes, K., S.-C. Tsay, W. Wiscombe, and K. Jayaweera, Numerically stable algorithm for
831 discrete ordinate method radiative transfer in multiple scattering and emitting layered media.
832 *Applied Optics*, **27**, 2502-2509, 1988.

833 Stamnes, P., J. F. de Haan, and J. W. Hovenier, The polarized internal radiation field of a planetary
834 atmosphere. *Astron. Astrophys.*, **225**, 239-259, 1989.

835 Stamnes, K., S-C. Tsay, W. Wiscombe, and I. Laszlo. DISORT: A general purpose Fortran
836 program for discrete-ordinate-method radiative transfer in scattering and emitting media.
837 Documentation Methodology Report, ftp://climate.gsfc.nasa.gov/wiscombe/Multiple_scatt/,
838 2000.

839 Van Roozendaal, M., Y. Wang, T. Wagner, S. Beirle, J.-T. Lin, N. Krotkov, P. Stamnes, P. Wang,
840 H. J. Eskes, and M. Krol. Structural uncertainty in air mass factor calculation for NO₂ and HCHO
841 satellite retrievals, *Atmos. Meas. Tech.*, **10**, 759–782, <https://doi.org/10.5194/amt-10-759-2017>,
842 2017.

843 Vermote, E. F., D. Tanré, J. L. Deuzé, M. Herman, and J. J. Morcrette. Second simulation of the
844 satellite signal in the solar spectrum, 6S: an overview. *IEEE Trans. Geosci. Remote Sens.*, **35**, 675–
845 686, 1997.

~~846 Vermote, E., N. Z. El Saleous, and C. O. Justice. Atmospheric correction of MODIS data in the
847 visible to middle infrared: First results. *Remote Sens. Environ.*, **83**(1/2), 97–111, 2002.~~

848 Vermote, E., C. O. Justice and F. -M. Bréon. Towards a Generalized Approach for Correction of
849 the BRDF Effect in MODIS Directional Reflectances. *IEEE Transactions on Geoscience and
850 Remote Sensing*, **47**(3), 898-908, doi: 10.1109/TGRS.2008.2005977, 2009.

851 Vestrucci, M., and C. E. Siewert, A numerical evaluation of an analytical representation of the
852 components in a Fourier decomposition of the phase matrix for the scattering of polarized light,
853 *JQSRT*, **31**, 177-183, 1984.

854 Walthall, C .L.; J. Norman, J. Welles, G. Campbell, and B. Blad. Simple equation to approximate
855 the bidirectional reflectance from vegetative canopies and bare soil surfaces. *Appl. Opt.* **24**, 383-
856 387, (1985).

857 Wanner, W.; X. Li, A. H. Strahler. On the derivation of kernels for kernel-driven models of
858 bidirectional reflectance. *J. Geophys. Res.*, **100**, 21077-21089, 1997.

859 Wanner, W.; Strahler, A.H.; Hu, B.; Lewis, P.; Muller, J.P.; Li, X.; Schaaf, C.L.B.; Barnsley, M.J.
860 Global retrieval of bidirectional reflectance and albedo over land from EOS MODIS and MISR
861 data: theory and algorithm. *J. Geophys. Res.*, **102**, 17143-17161, 1997.

862 Yang, Q., X. Liu, and W. Wu. A Hyperspectral Bidirectional Reflectance Model for Land Surface,
863 *Sensors* **20**(16), 4456; <https://doi.org/10.3390/s20164456>, 2020.

864

Formatted: Strikethrough